Seismic behavior and failure modes of non-ductile three-story reinforced concrete structure: A numerical investigation

Banu A. Hidayat[1,2a], Hsuan-Teh Hu[1,3b], Fu-Pei Hsiao[*1,4], Ay Lie Han[2], Lisha Sosa[1],
Li-Yin Chan[1] and Yanuar Haryanto[1,5]

[1]*Department of Civil Engineering, College of Engineering, National Cheng Kung University,*
No. 1 University Road, Tainan, 701, Taiwan R.O.C.
[2]*Department of Civil Engineering, Faculty of Engineering,   Universitas Diponegoro,*
Jalan Prof. Soedarto, Tembalang, Semarang, 50275, Indonesia
[3]*Department of Civil and Disaster Prevention Engineering, College of Engineering and Science, National United University,*
No. 2, Lien Da, Nan Shih Li, Miaoli, 36063, Taiwan R.O.C.
[4]*National Center for Research on Earthquake Engineering, 200 Sec. 3, Xinhai Road, Taipei, 10668, Taiwan R.O.C.*
[5]*Department of Civil Engineering, Faculty of Engineering, Jenderal Soedirman University,*
Jalan Mayjen. Sungkono KM 5, Blater, Purbalingga, 53371, Indonesia

Abstract.   Reinforced concrete (RC) buildings in Taiwan have suffered failure from strong earthquakes, which was magnified by the non-ductile detailing frames. Inadequate reinforcement as a consequence of the design philosophy prior to the introduction of current standards resulted in severe damage in the column and beam-column joint (BCJ). This study establishes a finite element analysis (FEA) of the non-ductile detailing RC column, BCJ, and three-story building that was previously tested through a tri-axial shaking table test. The results were then validated to laboratory specimens having the exact same dimensions and properties. FEA simulation integrates the concrete damage plasticity model and the elastic-perfectly plastic model for steel. The load-displacement responses of the column and BCJ specimens obtained from FEA were in a reasonable agreement with the experimental curves. The resulting initial stiffness and maximum base shear were found to be a close approximation to the experimental results. Also, the findings of a dynamic analysis of the three-story building showed that the time-history data of acceleration and displacement correlated well with the shaking table test results. This indicates the FEA implementation can be effectively used to predict the RC frame performance and failure mode under seismic loads.

Keywords: finite element analysis; concrete damage plasticity; non-ductile detailing; acceleration; displacement

1. Introduction

Many strong earthquakes hit Taiwan, as it is located in the Circum-Pacific seismic belt, resulting in thousands of reinforced concrete (RC) structures collapsing and thousands of casualties. The damage of the high-rise RC buildings was magnified by the non-ductile detailing design of structural members, as well as the inadequate reinforcement in the column and the lack of anchorage in the beam-column joints (BCJs) (Tsai *et al*. 2000, Tsai and Lin 2002, Yen and Chien 2004, Bechtoula and Ousalem 2005, Zepeda and Hagen 2016, Ghasemitabar *et al*. 2020). The experiences have led to increased awareness of the vulnerabilities of many RC structures, ranging from severe damage to complete collapse. These catastrophic

vulnerabilities have demonstrated the need for evaluating the seismic adequacy of existing buildings and to consider stricter seismic design codes for newly designed and constructed buildings (Tien *et al*. 2002, Otani 2004, Tudjono *et al*. 2015, Tudjono *et al*. 2018, Hidayat *et al*. 2019, Kepenek *et al*. 2020). In addition to policies that are already in effect, safe building design can be further enhanced through accurate structural analysis, especially in areas of high seismicity.

Undoubtedly, one of the most widely used materials in construction is concrete, due to its durability and constructability. There are two failure mechanisms in concrete: cracking under tension and crushing under compression. Bonding between the aggregate and the cement paste results in a greater compressive force than the tensile force (Mindess *et al*. 2003). Consequently, this low tensile strength promotes cracking at lower stresses than the compression stress. The overall stiffness of the material is reduced as the micro cracking propagates through the cement paste, and the unrecoverable plastic deformation is encountered. When the steel reinforcement is embedded in concrete and begins to yield at the cracks, the stresses in the rebar between the cracks will be less than the yield stress on the cracks because parts of the tensile force are resisted by

---

∗Corresponding author, Researcher Fellow
  E-mail: fphsiao@ncree.narl.org.tw
[a]Ph.D. Candidate
  E-mail: banuardihidayat@lecturer.undip.ac.id
[b]Professor
  E-mail: hthu@ncku.edu.tw

the concrete (Wang *et al.* 2008). The aggregate interlock and the dowel action also contributes the crack development on concrete (Kataoka *et al.* 2020). Furthermore, during an actual earthquake with real ground acceleration, the beams and columns of structures experience shear forces and rapid periods of tension and compression stresses.

The nonlinear material behavior of concrete can be attributed to two distinct mechanical phenomena: damage and plasticity (Cicekli *et al.* 2007). Consequently, a model that accounts for both plasticity and damage is necessary and adopted to the finite element analysis (FEA) model. Thus, this research focused on the FEA modeling to show more detailed seismic performance and structural behavior of the non-ductile and poorly designed three-story RC building, including the column and BCJ members, using ABAQUS software. The FEA results are then being compared to the shaking table and quasi-static test results. The analysis combines the damage plasticity model for concrete and the elastic-perfectly plastic model for steel reinforcement.

This study is a part of the whole research project (Shen *et al.* 2018, Shen *et al.* 2019, Hidayat *et al.* 2020, Lin *et al.* 2020) conducted in the National Center for Research on Earthquake Engineering (NCREE) Laboratory in Tainan City, Taiwan. The research work refers to the shaking table test of a three-story RC frame structure scaled down to 50%, which is based on the Weiguan Jinlong building in Tainan City. The building was constructed in 1995 with non-ductile and non-seismically designed characteristics, and it collapsed during the 2016 Mei-Nong earthquake. The damage of the building generally occurred in the BCJ components, followed by excessive damage of the columns in the first floor with higher story height and larger opening which led to the lower structural stiffness and strength.

2. Finite element modeling

2.1 Constitutive material models

The longitudinal and stirrup reinforcement used in this study was ASTM A-706 Grade 60 steel of a 19-millimeter diameter with a yielding stress of σ_y=455 MPa and ASTM A-615 Grade 40 steel of a 10-millimeter diameter with a yielding stress of σ_y=355 MPa, respectively. For both steels, a Poisson's ratio of v_c=0.3 and the elastic modulus of E_s=200 GPa were assumed.

The concrete had a uniaxial compressive strength of f'_c=20.7 MPa measured experimentally through compressive strength tests at 28 days. The modulus of elasticity and Poisson's ratio are the two values which describe the linear elastic behavior of concrete. For this RC column and BCJ study, a Poisson's ratio of v_c=0.2 was assumed. Likewise, the modulus of elasticity was estimated according to ACI-318 code (American Concrete Institute 2019) and reduced by 20% in accordance with Taiwan Code (Ministry of the Interior 2019), as mentioned in Eq. (1).

$$E_c = 0.8 \times 4{,}700 \sqrt{f'_c} = 0.8 \times 4{,}700\sqrt{20.7} \qquad (1)$$
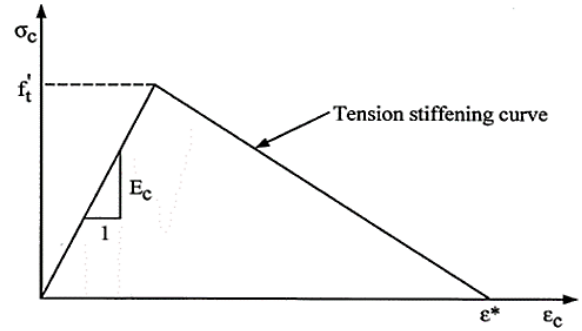$$= 17{,}107 \, MPa$$

Fig. 1 Concrete's tension stiffening model

As the concrete is relatively weak and brittle in tension, the interactions between the cracked concrete and steel can cause highly nonlinear behavior (Hu and Schnobrich 1990, Haryanto *et al.* 2019). Thus, defining the nonlinearity requires precise definition of three components: plasticity, tensile behavior, and compressive behavior.

The concrete constitutive model in ABAQUS uses the concrete damage plasticity (CDP) concept. The tensile behavior can be adequately described by defining tension stiffening and tension damage data. In this case, a simple descending line was used to model the tension stiffening phenomenon (Dassault Systemes 2011) with the strain value at which the tensile stress goes to zero being ε'=0.001, as shown in Fig. 1. Therefore, the tensile strength for normal weight concrete according to the ACI code (2019) can be described as Eq. (2).

$$f'_t = 0.25 \sqrt{f'_c} = 0.25\sqrt{20.7} = 1.14 \, \text{MPa} \qquad (2)$$

The mechanical behavior under uniaxial loading for tension can be characterized by damage plasticity in Fig. 2 (Dassault Systemes 2011). Under uniaxial tension, the stress-strain curve initially follows a linear elastic path up to the failure stress, σ_{t0}. This point marks the beginning of microcracking which results in a softening behavior. If the concrete is being unloaded from any point on the softening post-peak portion of the curve, then the elastic modulus will be weakened due to damage. The damage factor, d_t, represents the rate of stiffness degradation and formulated in Eq. (3), which can take values from 0, meaning undamaged, to 1, meaning a total loss of strength.

$$\sigma_t = (1 - d_t)E_0\left(\varepsilon_t - \varepsilon_t^{pl}\right) \qquad (3)$$

where E_0 is the undamaged modulus of elasticity and $\varepsilon_t{}^{pl}$ is the tensile plastic strain.

The compressive behavior in the CDP model can be fully described by a compression hardening/softening rule (Yu *et al.* 2010) and the compression damage data, which can be neglected due to the little effect of the compressive damage parameter under the static monotonic loading (Hany *et al.* 2016). For this study, the equation used to define the stress-strain relation of concrete under uniaxial compression is shown in Eqs. (4) and (5).

$$f_c = \frac{E_c \varepsilon_c}{1 + (R + R_E - 2)\left(\frac{\varepsilon_c}{\varepsilon_o}\right)^2 - (2R - 1)\left(\frac{\varepsilon_c}{\varepsilon_o}\right)^2 + R\left(\frac{\varepsilon_c}{\varepsilon_o}\right)^3} \qquad (4)$$
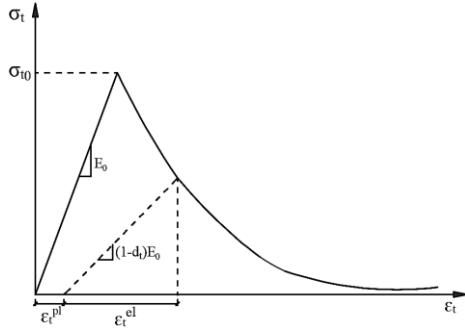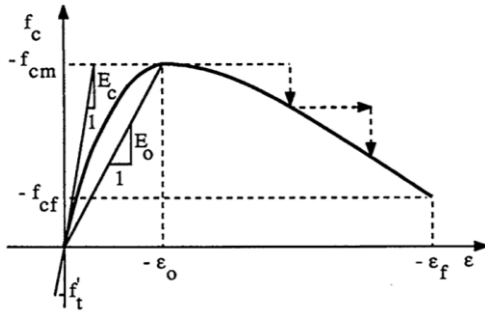
Fig. 2 Response of concrete to uniaxial loading in tension

Fig. 3 Concrete compression's stress-strain curve

Table 1 The plasticity parameters for the CDP model

ψ	e	f_{b0}/f_{c0}	K	viscosity
38	0.1	1.16	0.667	0.00001

$$R = \frac{R_E(R_\sigma-1)}{(R_\varepsilon-1)^2} - \frac{1}{R_\varepsilon} \quad R_E = \frac{E_c}{E_o} \quad E_o = \frac{f_{cm}}{\varepsilon_o}$$
$$R_\sigma = \frac{f_{cm}}{f_{cf}} \quad R_\varepsilon = \frac{\varepsilon_f}{\varepsilon_o} \tag{5}$$

where f'_c is the compressive stress at each point on the graph; E_c is the initial modulus of elasticity for concrete; E_o is the secant modulus of elasticity; f_{cm} is the degraded maximum compressive strength corresponding to $f_{cm}=0.9$ f'_c; ε_f is the maximum compressive strain on the uniaxial stress-strain curve; f_{cf} is the stress corresponding to ε_f on the uniaxial stress-strain curve; and ε_o is the strain corresponding to f_{cm}. To obtain values for f_{cf} and ε_f, it is assumed that $R_\sigma=4$ and $R_\varepsilon=4$ in accordance with Hu and Schnobrich (1990). Fig. 3 shows the stress-strain curve for concrete compression (Saenz 1964).

The plasticity parameters used in this study are shown in Table 1. The dilation angle ψ is measured in the *p-q* (deviatory) plane at high confining pressure with the value based on Jankowiak and Lodygowski (2005); e is the eccentricity of plastic potential, f_{b0}/f_{c0} is the ratio of the initial biaxial to initial uniaxial compressive strength; K is the ratio between the magnitudes of deviatoric stress in uniaxial tension and compression based on a triaxial test; and viscosity is used for the viscoplastic regularization of the concrete constitutive equations in ABAQUS analyses (Ma *et al*. 2018).

Furthermore, in the attempt to obtain good FEA results, a simpler idealized material model was used. The concrete model chosen was a CDP model, which does not consider

Table 2 Details of RC members in three-story building model

Elements		Width (m)	Length (m)	Height (m)
Column A at first floor	CA1	0.3	0.3	3
Column A at upper floors	CA2	0.3	0.3	1.5
Column B at first floor	CB1	0.3	0.75	3
Column B at upper floors	CB2	0.3	0.75	1.5
Beam between CA	B1	0.3	3.2	0.4
Beam between CB	B2	0.3	2.75	0.4
Slab	SL	3.2	3.2	0.1
Wall	WA	1.1	3.2	0.15

Table 3 Details of concrete and steel elements in the column and BCJ models

Elements	Width (cm)	Length (cm)	Height (cm)	Hook (cm)	Diameter (cm)
Column model					
Concrete elements					
C-A	30	30	130	-	-
C-B	30	75	130	-	-
Steel elements					
C-A: Longitudinal bar	-	-	130	-	1.91
C-A: Stirrup	19.9	19.9	-	-	0.95
C-B: Longitudinal bar	-	-	130	-	1.91
C-B: Stirrup	19.9	64.9	-	-	0.95
BCJ model					
Concrete elements					
C-A	30	30	475	-	-
C-B	30	75	475	-	-
Beam	25	40	130	-	-
Steel elements					
C-A: Longitudinal bar	-	-	475	-	1.91
C-A: Stirrup	19.9	19.9	-	-	0.95
C-B: Longitudinal bar	-	-	475	-	1.91
C-B: Stirrup	19.9	64.9	-	-	0.95
Beam: Top longitudinal bar	-	-	155	30	1.91
Beam: Bottom longitudinal bar	-	-	150	30	1.91
Beam: Stirrup	14.9	29.9	-	-	0.95

the strain softening. Meanwhile, the constitutive model of the steel reinforcements was implemented based on the elastic-perfectly plastic model. However, the reliability of the results relies on the accuracy of the materials' constitutive models (Suwada and Fukuyama 2006). Also, modeling uncertainties and assumptions can influence the structural performance, i.e., the load-bearing capacities, failure modes, seismic resistance, and shear stiffness of the structural members (Celarec and Dolšek 2013, Holický *et al*. 2016, Castaldo *et al*. 2019, Castaldo *et al*. 2020).

In ABAQUS, the E_o value was used to determine the modulus of elasticity of the concrete materials, as mentioned in Fig. 3, instead of using the value of E_c, so that the values of E_o=6,900 MPa and E_o=3,800 MPa are used, respectively, for the RC components and RC building. The modulus of elasticity of the concrete and the steel

C-A 30×30 cm   C-B 30×75 cm   Beam 25×40 cm

Plan view of the building floor   Side view of the building
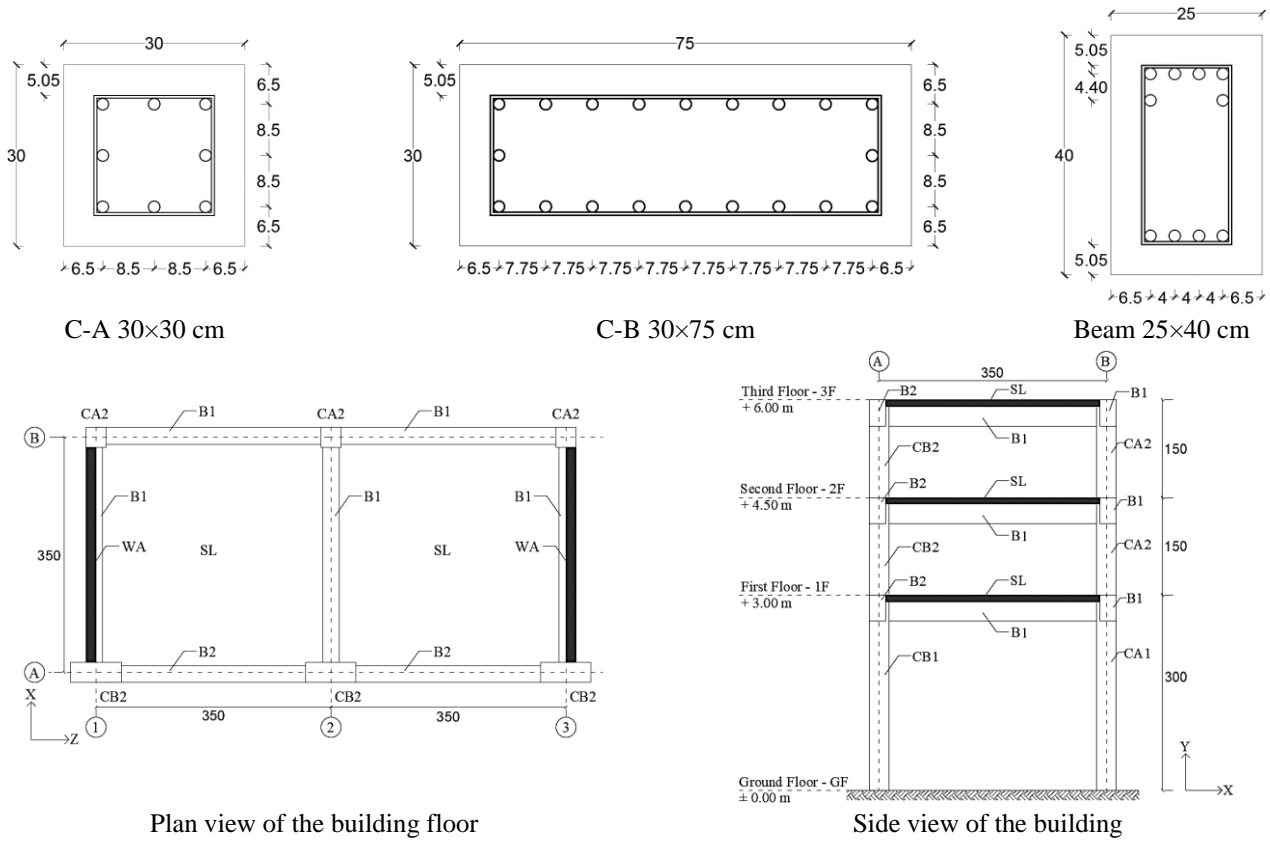
Fig. 4 The cross-sectional details of the RC specimen models (size in cm)

reinforcement for the three-story building was reduced by 45% to match the fundamental natural period and the Rayleigh damping coefficients of the experimental results, which in turn changed the yielding strains.

2.2 Specimen models

In this study, a half-scale three-story RC building and two types of RC columns and BCJs were considered to be modeled in ABAQUS software. The columns were differentiated in the cross-sectional areas, the small column denoted as C-A and the large column as C-B, yet having the same length. For the BCJ specimens, the two types of the column were connected to the RC beam with the same area and length, labeled as BCJ-A and BCJ-B, respectively. The specimen model was originally taken from the non-ductile column and BCJ prototypes tested in the quasi-static test (Hidayat *et al*. 2020) and the building specimen tested in the shaking table test (Shen *et al*. 2018, Lin *et al*. 2020), including the exact same dimensions, material properties, and rebar configurations. The member details of the three-story building and the column and BCJ specimens are presented in Tables 2 and 3, respectively. Fig. 4 shows the plan view and cross-section of the models.

However, some assumptions were adjusted to simplify the numerical model. The interaction between the steel reinforcements and the concrete was assumed to be in the perfect bonding condition. The RC foundations and the cross-tie reinforcement were not considered. Thus, the dynamic loading was given by using the X-direction acceleration recorded at the shaking table test, rather than the three-dimensional acceleration in three directional, because the greatest amplitude was in the X-direction.

To accurately model the single curvature behavior of the column specimens, the FEA simulation only took the half-height of the column with the bottom part fixed and the top end free and unconstrained. This simplification was taken since the base shear obtained from the quasi-static test was twice as big as a result of the double curvature behavior. Meanwhile, the BCJ simulation model used the same condition of the quasi-static experimental program. The lateral monotonic loading was also applied in the model and replaced the quasi-static loading as in the experimental program, due to the envelope curve being independent of loading history and fits reasonably well with the load-displacement curve under monotonic loading.

The RC components were modeled in ABAQUS as 3D deformable solid elements, whereas the steel reinforcement was a 3D deformable truss element. The element type used to discretize the concrete was the 8-node solid element with reduced integration or C3D8R to prevent the shear locking effect. Also, the compression hardening and tension stiffening of the concrete can be well-modeled (Islam, 2020). This C3D8R element has three degrees of freedom (DoF), the translations in the X, Y, and Z directions, for each node. The rebar was modeled by 2-node truss elements or T3D2, which has three DoF for each node, the translations in the X, Y, and Z directions. By doing a mesh sensitivity study, an appropriate mesh with the seed size of 5 cm was found. The steel and concrete were meshed
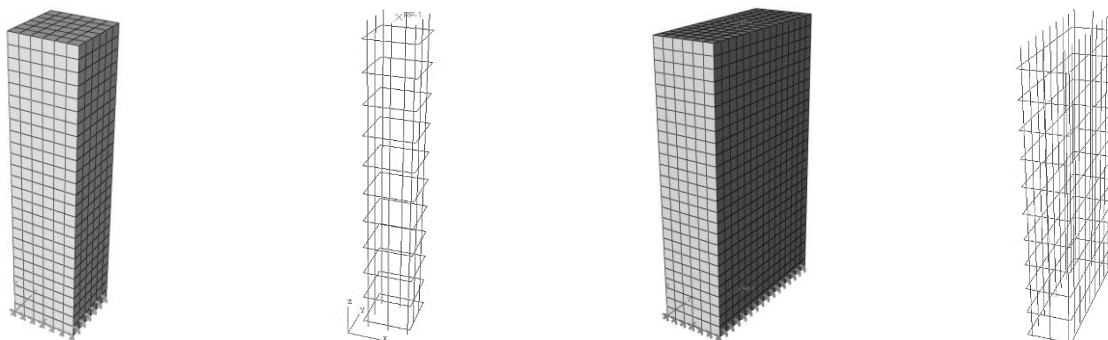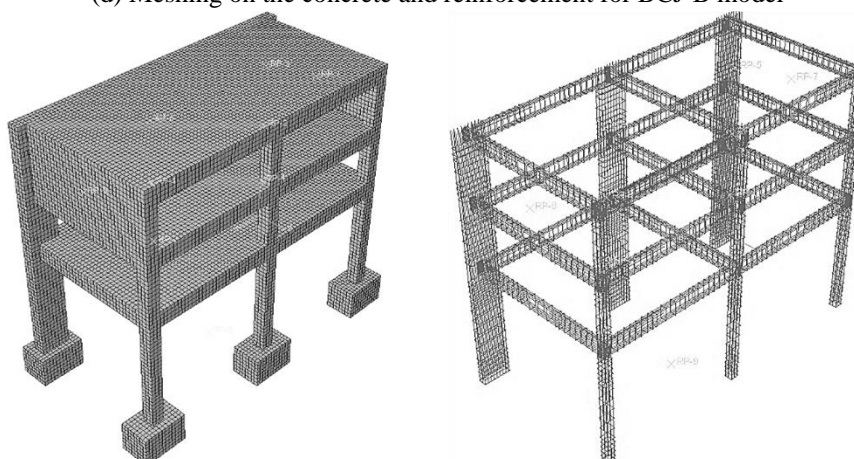
(a) Meshing on the concrete and reinforcement for C-A model (b) Meshing on the concrete and reinforcement for C-B model
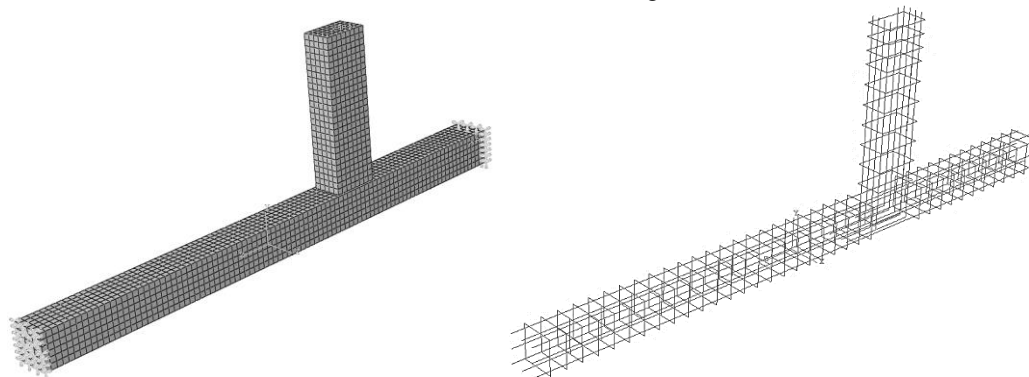
(c) Meshing on the concrete and reinforcement for BCJ-A model
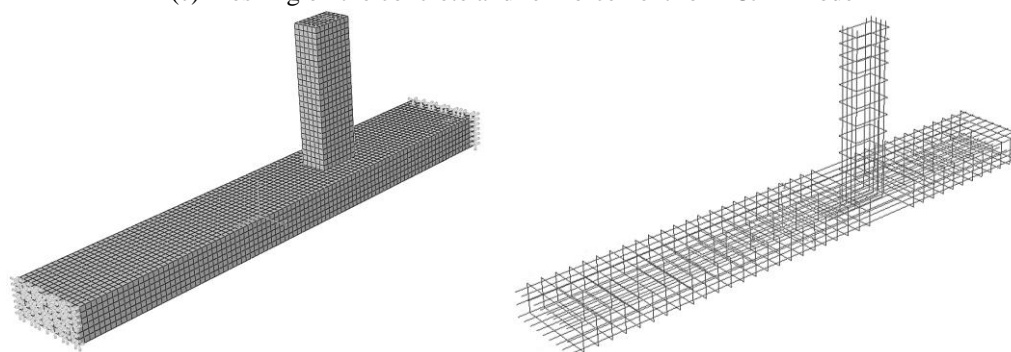
(d) Meshing on the concrete and reinforcement for BCJ-B model

(e) Meshing on the concrete and reinforcement for three-story building model

Fig. 5 The meshing distribution of the RC specimens

together as one assembly rather than as individual parts. Fig. 5 depicts the details of the FE mesh and Table 4 compiles the final meshing for each model.

2.3 Loading and boundary condition

In the column and BCJ analysis, the static linear

Table 4 The final meshing usage for the numerical models

Element type	C3D8R	T3D2
C-A	936	384
C-B	2,340	894
BCJ-A	4,460	2,266
BCJ-B	9,590	4,216
Three-story building	25,300	18,228

analysis by choosing the 'Static General' step was done using a time period of 1 along with 100 maximum increments and an initial increment size of 0.1. This step uses Newton's method as the solver and, however, it cannot produce a curve beyond the yielding point. Therefore, to analyze the static nonlinear case of the model, the 'Static Riks' step was chosen, due to its efficiency in predicting the

behavior of unstable structures having large deformation and to provide a curve beyond the yield point. This approach involves the load proportionality factor and displacement at each time increment. The increment size is found by iterating through the arc length until convergence occurs. (Dassault Systemes 2011).

However, for the RC building, the 'Linear Perturbation-Frequency' step was used in the linear case, and the 'Dynamic Implicit' method by using the Hilber-Hughes-Taylor operator was chosen for the nonlinear analysis. It uses the general direct-integration method and the extension of the trapezoidal rule. As the Hilber-Hughes-Taylor operator is implicit, the integration operator matrix must be inverted and a set of simultaneous nonlinear dynamic equilibrium equations must be solved at each time increment. This solution is done iteratively to achieve the quadratic convergence by using Newton's method (Dassault
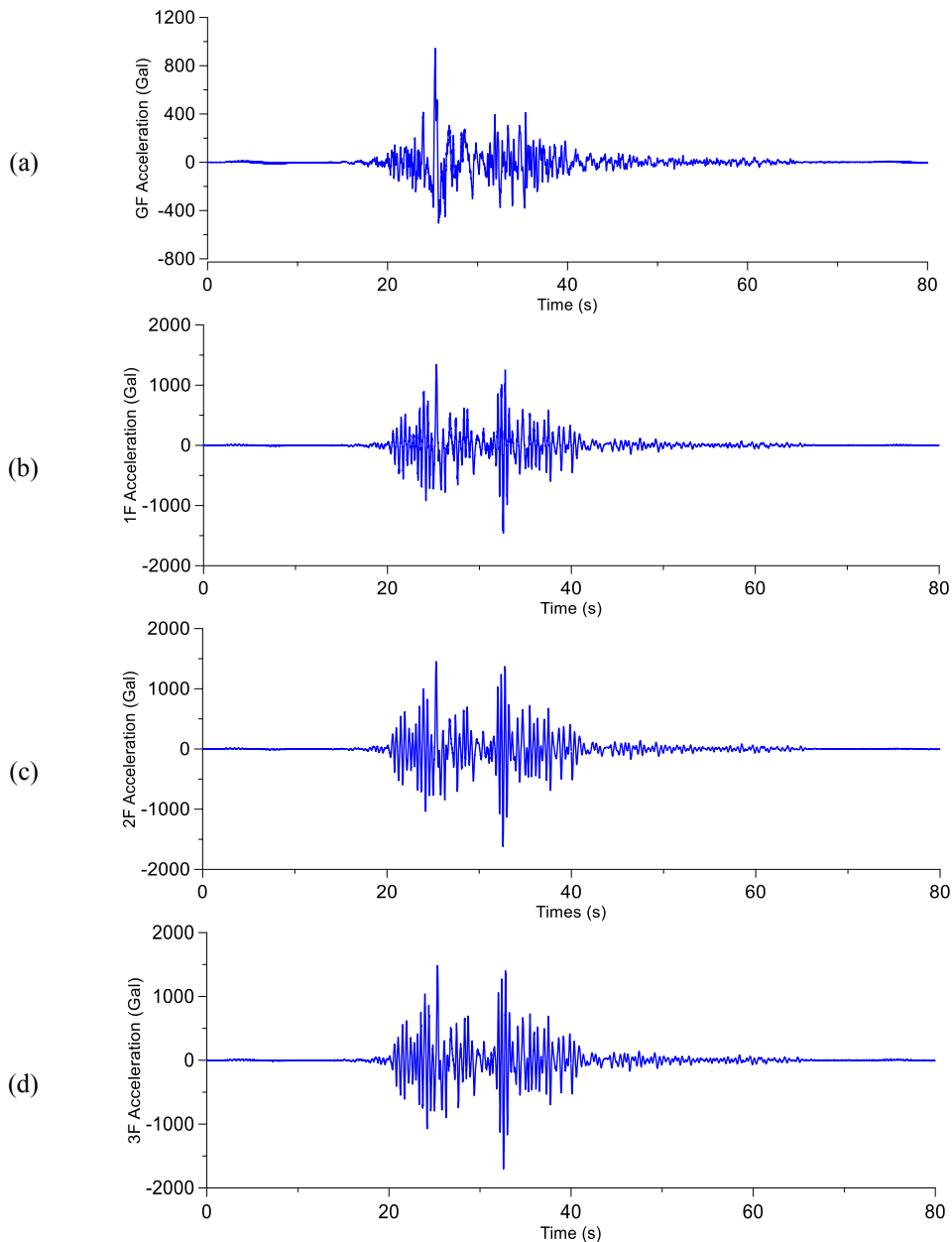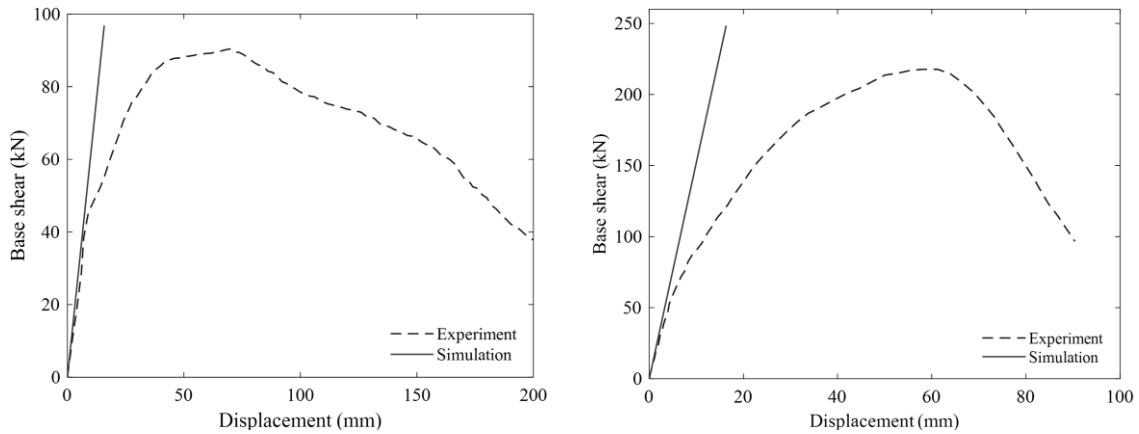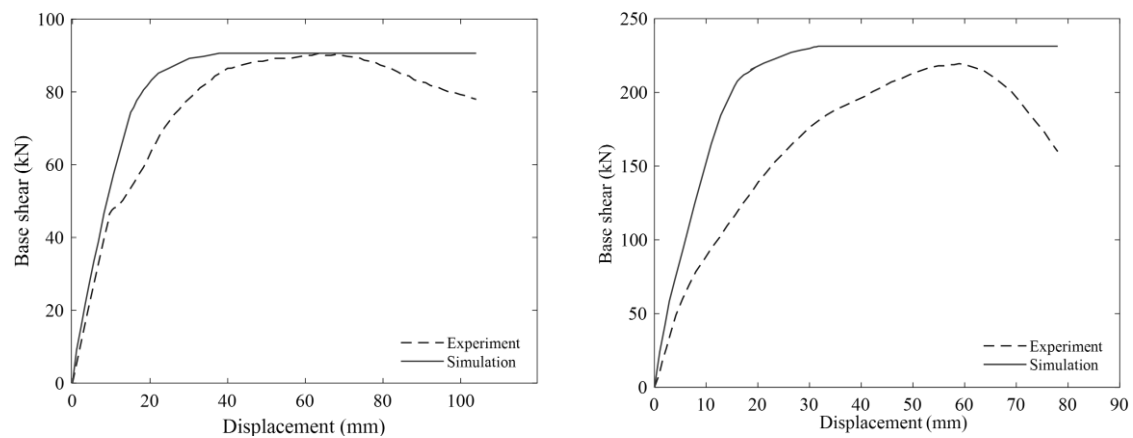

Fig. 6 Measured acceleration at each floor during the 800 Gal shaking table test

(a) The load-displacement graph of C-A

(b) The load-displacement graph of C-B

Fig. 7 The load-displacement curve of the linear analysis in the column specimens

(a) The load-displacement graph of C-A

(b) The load-displacement graph of C-B

Fig. 8 The load-displacement curve of the nonlinear analysis in the column specimens

Systemes 2011).

To display the single curvature behavior in the column, a fixed boundary condition was applied to the bottom of the column using a controlling reference point located at the column's bottom surface center point. The reference points were made to interact with the column surfaces as rigid bodies. The unidirectional concentrated force was put to the reference point at the top of the column with the maximum lateral load measured in the experimental program, which is 96.86 kN for the C-A and 225.24 kN for the C-B.

However, for the BCJ model, the column and beam are established and then combined to each other by using the tie command. The purpose is to make the displacement and rotation angle of the two interfaces in the same direction and to define the two components as the concrete frame system. As the RC foundation was not set in the BCJ model, the two ends of the column should be in the fixed condition. In addition, the beam end surface is constrained to the reference point, and the maximum lateral load applied is 100.40 kN and 157.47 kN for the BCJ-A and BCJ-B, respectively. The boundary condition details of column and BCJ models are also shown in Fig. 5.

The three-story building model adopted the pin connection and acceleration amplitude applied as the boundary conditions to the bottom surfaces of all columns.

For the dynamic analysis, the acceleration was directly applied in the X-direction with the constrained translation in the Y- and Z-directions. The input base ground acceleration was the acceleration time history recorded on the shaking table, as shown in Fig. 6, which was the 800 Gal seismic force of the TCU052 station. This ground motion was taken from the 1999 Chi-Chi earthquake and can be classified as the near-fault ground motion. However, the time duration of the base ground acceleration was reduced as the three-story building tested in the shaking table test was scaled down to 50%.

3. Results and discussion

3.1 Column specimens

At the first step, the linear analysis of the column components was performed, which means using only the Young's modulus and Poisson's ratio to define the concrete and steel materials. Fig. 7 shows the resulting FEA linear curve against the experimental envelope curve of the quasi-static test for the C-A and C-B specimens. Using the secant modulus (E_o) indeed softened the curve enough so that it coincided well with the elastic part of the experimental
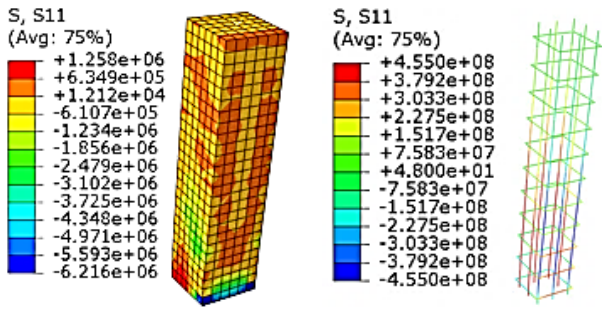
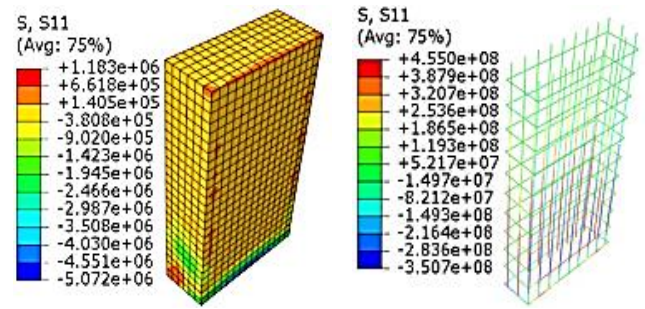(a) Distribution of principal stress in the X-direction
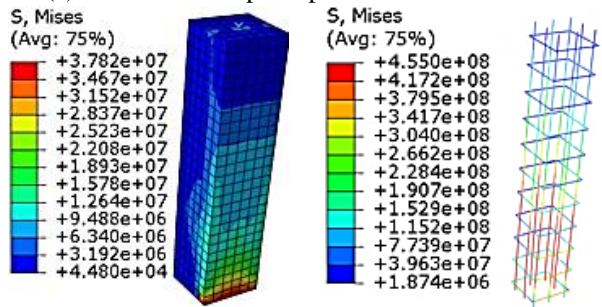
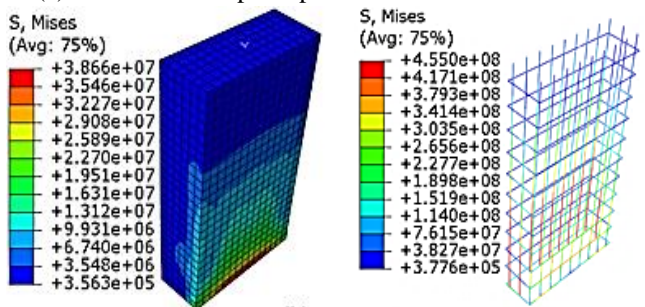(b) Distribution of Von Misses stress
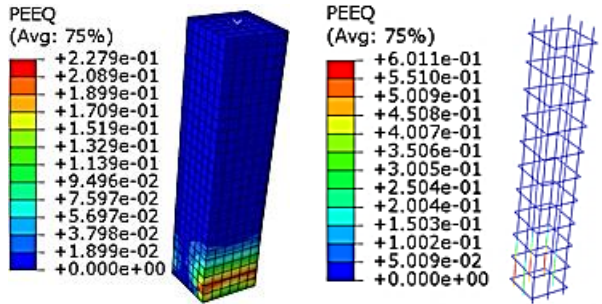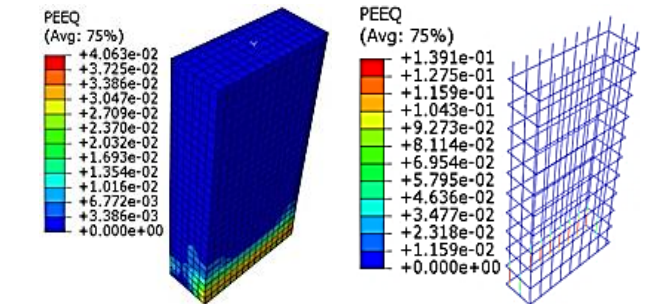

(c) Distribution of equivalent plastic strain

Fig. 9 ABAQUS output stress and plastic strain for C-A specimen

(a) Distribution of principal stress in the X-direction

(b) Distribution of Von Misses stress

(c) Distribution of equivalent plastic strain

Fig. 10 ABAQUS output stress and plastic strain for C-B specimen

curve. The deflection and stiffness of the FEA results are also comparable to experimental envelope curves. By comparing the simulation and experimental results in Figs. 7(a)-(b), it can be seen that the coincidence degree of the C-A specimen is better than that of C-B specimen.

However, a nonlinear static analysis was conducted by applying a lateral monotonic load to the top of the columns using the 'Static Riks' step and the material nonlinearity parameters. To obtain a backbone curve, the resulting base shear versus the top column displacement curves were plotted. The interest of this study was more to see if the initial stiffness and the maximum base shear could be predicted within good accuracy between the FEA and experimental results, since the elastic-perfectly plastic model for the concrete and reinforcing bars was used.

It can be seen from Fig. 8 that FE simulation curves are initially linear then smoothly transition to the yield point and continue to be perfectly plastic without a reduction in strength. Yet, the experimental curve is measured with sensitive equipment that more accurately represents the brittle behavior of concrete. Furthermore, in observing the initial stiffness of the FEA curves, it compares well with experimental backbone curve. The peak of base shear for C-

A matches almost exactly, and for C-B the maximum base shear was within 10% of the measured value. This shows that the numerical model was adequate. As a result, the nonlinear analysis validated the material model so that it can be used in the dynamic analysis of the entire three-story building specimens.

A collapse prevention point was manually defined to set a limit on the maximum displacement in the graph, as shown in Fig. 8. By using the drift limit of 4% and 3% for the flexure-shear behavior as experienced by the C-A and C-B specimens, respectively, in the quasi-static test previously conducted by Hidayat *et al*. (2020). The limit was formulated by multiplying the drift limit value and the clear height of the columns, which is 2,600 mm, and the collapse prevention point can be found as 104 mm and 78 mm, respectively, for the C-A and C-B specimens

The principal stress in the X-direction, the Von Misses stress, and the equivalent plastic strains for the concrete column and reinforcement cage of the C-A specimen are depicted in Figs. 9(a)-(c), separately. However, Fig. 10 shows the identical result components for the C-B specimen. The principal stress in the X-direction is denoted by *S11* and represents the maximum possible tensile or

(a) C-A tensile damage model   (b) C-A compressive damage model   (c) C-A experimental

(d) C-B tensile damage model   (e) C-B compressive damage model   (f) C-B experimental
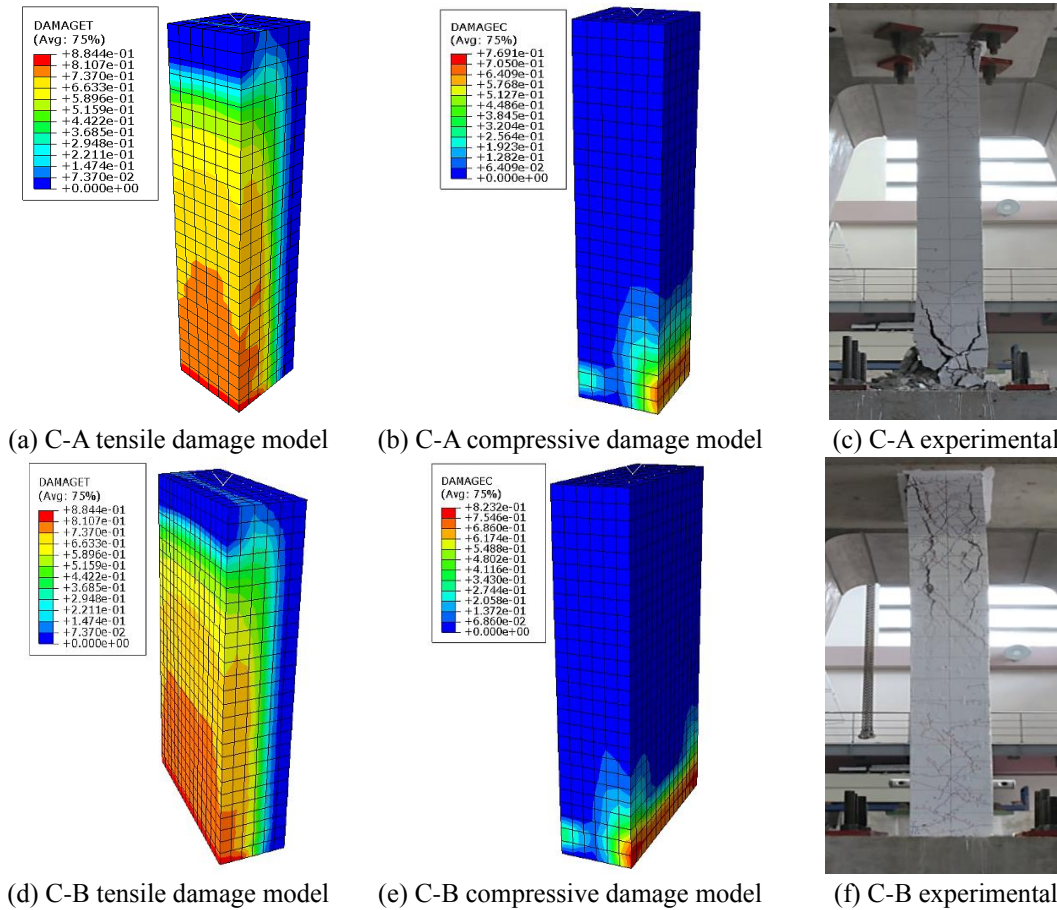
Fig. 11 Damage scenario of C-A and C-B specimens

compressive stress. The primary use of this principal stress is to predict failure in a structure which has a complex state of biaxial or triaxial stress, i.e., it can be used as the failure stress criterion for brittle material like concrete. This also visualizes the flow of stress in the structure.

On the other hand, the Von Misses stress is a function of the three principal stresses, it more accurately predicts failure for ductile materials like steel, and it is used to compare against the design stresses. The equivalent plastic strain gives a measure of the amount of permanent strain in the structure body. It can be seen from Figs. 9(c) and 10(c) that the permanent deformation occurred at the base of the columns. In addition, most of the tensile stress was absorbed by the reinforcing bars, especially at the bottom of the column on the tension side, where most of the stress was experienced. The stirrup bars also showed most of the stress at the bottom of the column as well.

The damage scenario of the numerical simulation and the quasi-static test are depicted in Fig. 11. Both results show that the most damaged parts of the specimens occurred at the column and the bottom base intersection. The simulation results show the damage scenario of the tensile and compressive stresses by the load given. By the experimental results (Hidayat *et al*. 2020), the C-A and C-B specimens failed in the axial flexural and shear failure modes, respectively.

3.2 BCJ specimens

In the load-displacement graph of this study, the loads are taken from the fixed position of the joints between the beam and the columns. Thus, the displacements are captured from the reference point in the beam's cross-section surface relative to the joint intersection. The numerical model results are then compared to the experimental results (Hidayat *et al*. 2020), as shown in Fig. 12.

At the first stage, the common points of the FEA curve are initially linear, as the stiffness in the elastic stage of the model is clearly visible, then smoothly transition to the point of undulation and decrease with the plasticity stage. Differences in the curve may be related to various external factors in the experimental test, the numerical model which is relatively conservative, and the strength has not yet developed completely into the plastic stage.

Comparing the numerical and experimental specimens from Fig. 13, as expected, the damage occurred at the beam-column joint. Although the results of BCJ analysis cannot fully meet the experimental data, it can be seen from the results that the damage response meets the design requirements and also the elasticity and plasticity behavior of BCJ specimens.
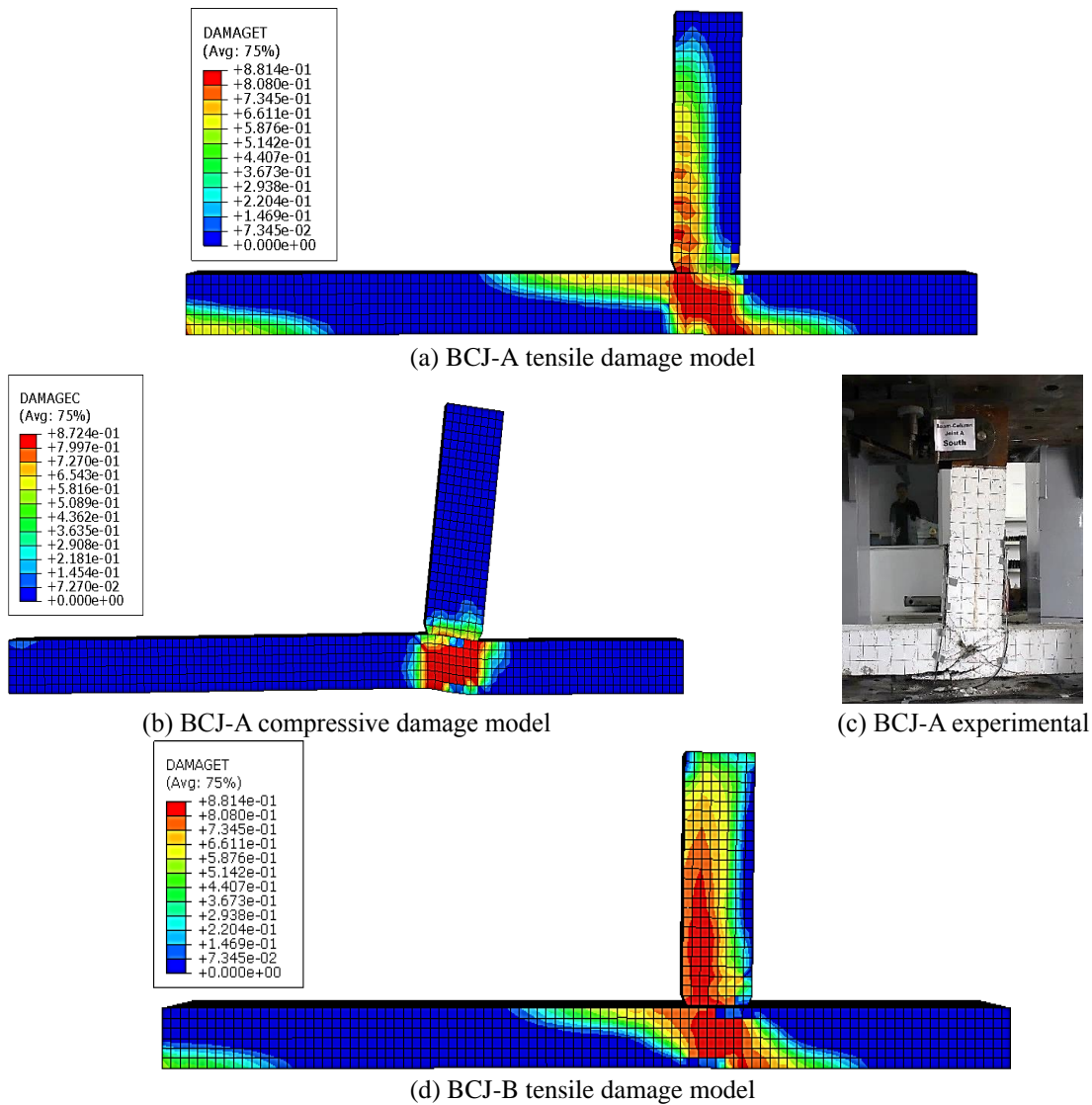
3.3 Three-story building specimens

3.3.1 Linear analysis
To simulate the dynamic behavior of the linear analysis
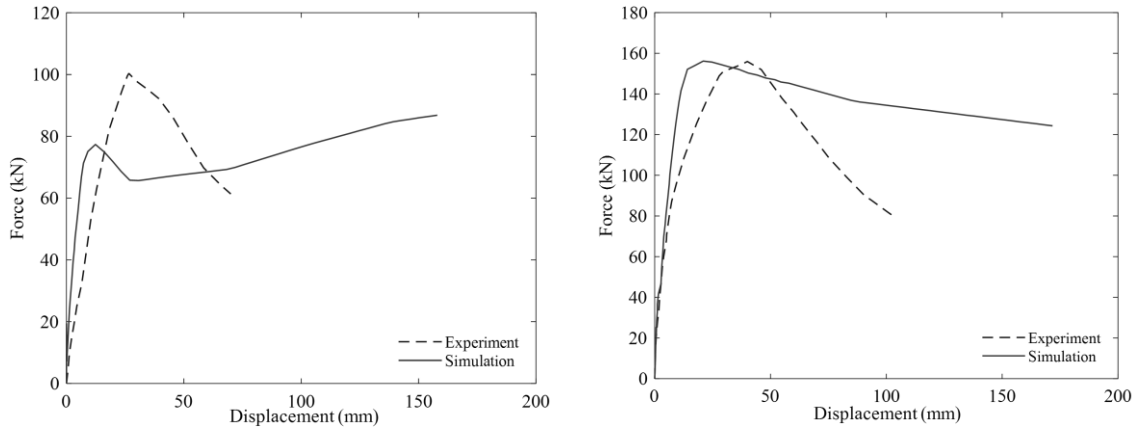
| (a) The load-displacement graph of BCJ-A | (b) The load-displacement graph of BCJ-B |

Fig. 12 The load-displacement curve of the BCJ specimens

(a) BCJ-A tensile damage model

(b) BCJ-A compressive damage model

(c) BCJ-A experimental

(d) BCJ-B tensile damage model

Fig. 13 Damage scenario of BCJ-A and BCJ-B specimens

of the three-story building, the gravity load was applied in the 'Static General' step, and the input base acceleration with a time period of 80 seconds, 0.02 as the initial increment size, and the total number of increments of 1,000

were chosen for the 'Dynamic Implicit' step. Fig. 14 shows the measurement points of acceleration and displacement in the model. The displacements and absolute accelerations at floor levels are two of the most significant global kinematic

(e) BCJ-B compressive damage model
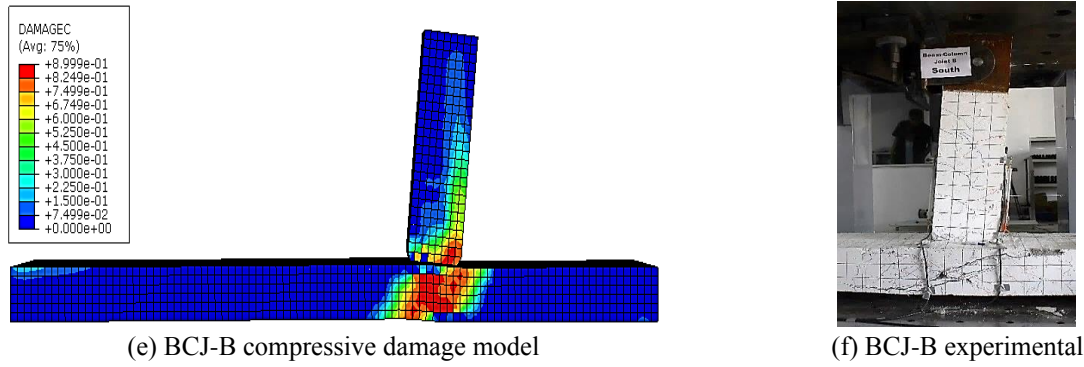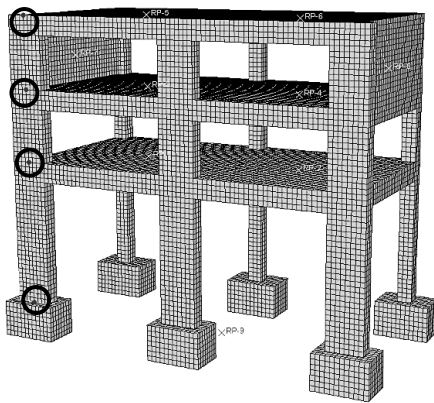
(f) BCJ-B experimental

Fig. 13 Continued

Fig. 14 The measurement points of acceleration and displacement

parameters that synthesize the dynamic response of a building. Consequently, Figs. 15 and 16 display the acceleration and displacement with respect to the ground level of time histories plotted against the experimental results (Shen *et al*. 2018; Lin *et al*. 2020) corresponding to the shaking table test with a nominal GPA of 0.94 g (800 Gal).

Both the acceleration and displacement time histories are well correlated with the measured data, and their amplitudes seem to be appropriately damped. The harmonic wave motions are also in phase with the experimental results mainly because the fundamental building period of the FEA was made to match that of the real RC building specimen. Furthermore, Table 5 presents the comparison of
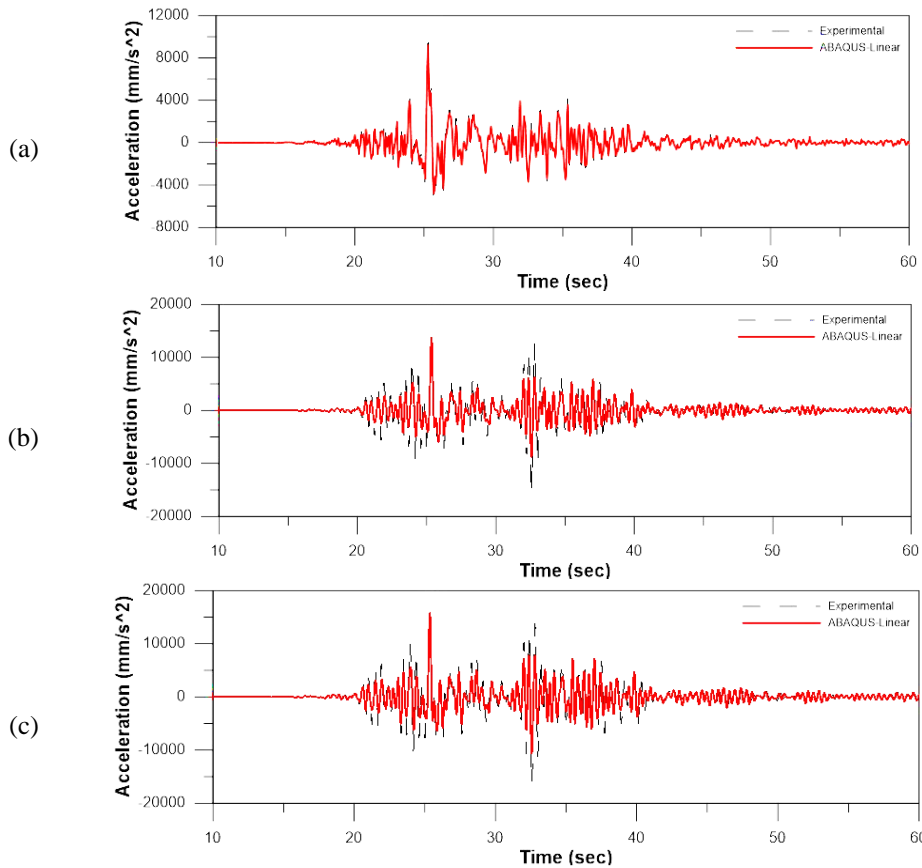

(a)

(b)

(c)

Fig. 15 Comparison of measured acceleration in linear analysis at (a) ground floor; (b) first floor; (c) second floor; and (d) third floor
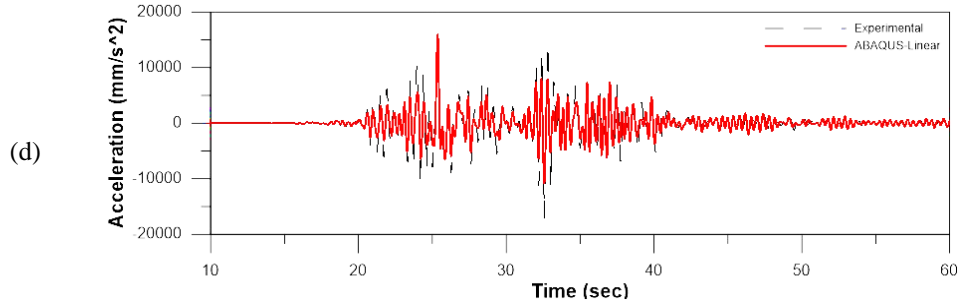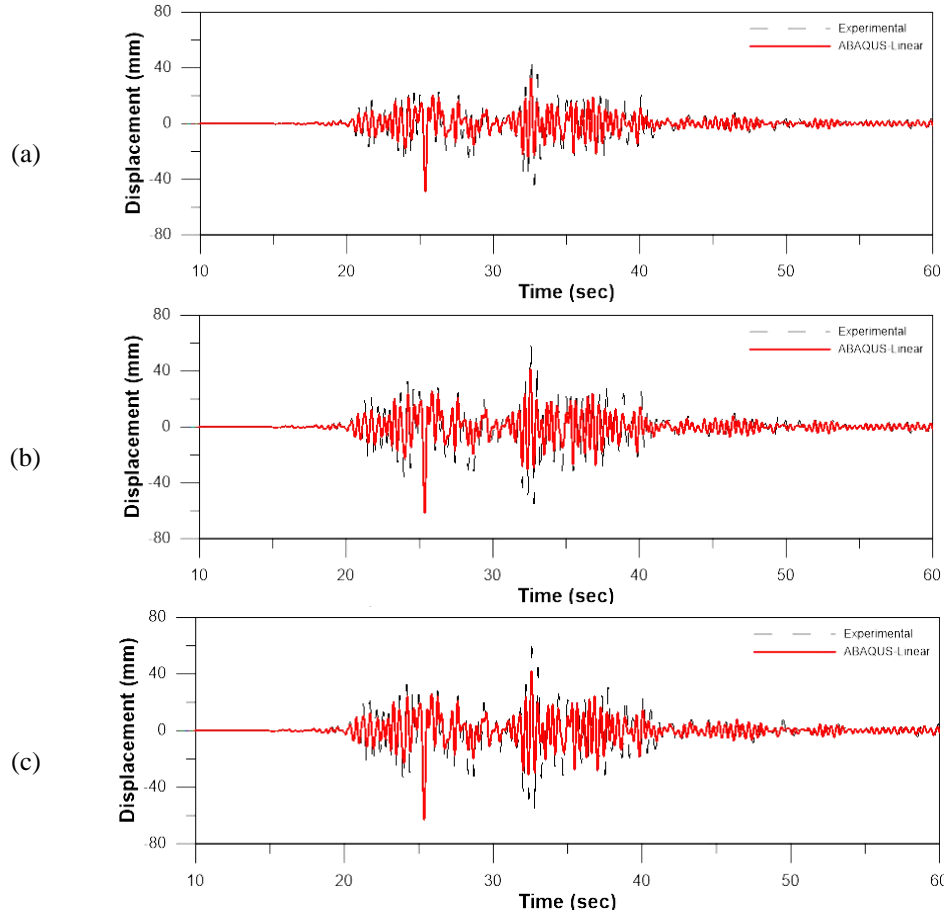
Fig. 15 Continued

Fig. 16 Comparison of relative displacement in linear analysis at (a) first floor; (b) second floor; and (c) third floor with the ground floor

Table 5 Comparison of linear dynamic FEA data to experimental data

| Floor level	Direction	Max Acceleration (mm/s^2)		Max Displacement (mm)	
		Experimental	FEA	Experimental	FEA
Ground floor	Positive	9,441	9,444	-	-
	Negative	5,050	5,048	-	-
First floor	Positive	13,450	13,706	48	32
	Negative	14,602	8,827	47	49
Second floor	Positive	14,528	15,741	59	41
	Negative	16,210	10,677	58	62
Third floor	Positive	14,842	15,907	59	42
	Negative	17,049	10,819	58	63

the maximum positive and negative amplitudes after excitation for the acceleration and displacement time histories. Table 5 shows that the normalized mean square error (NMSE) for all the three floor of the building specimen is 0.084 and 0.057, respectively for the maximum acceleration and maximum relative displacement. This analysis indicated that the comparison of the experimental and FEA results is in reasonable agreement.
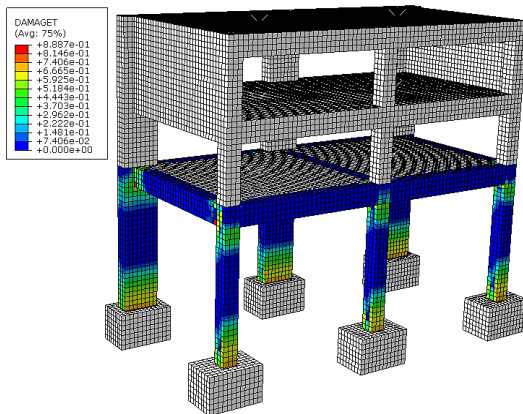
3.3.2 Nonlinear analysis

The nonlinear analysis was simulated by firstly applying a gravity load and later applying a base acceleration with a 80 seconds time period. A total increment number of 1,000 was employed, and 0.002 was chosen as the initial
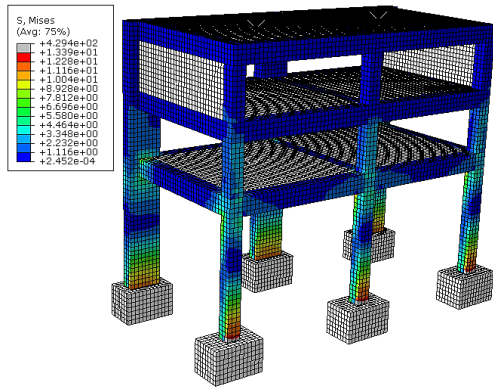
(a) Von Misses Stress distribution in concrete
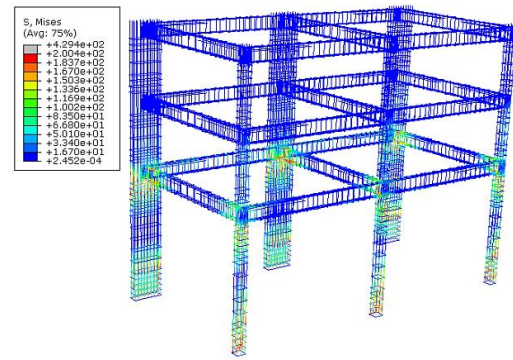
(b) Von Misses Stress distribution in rebar

(c) The tensile damage model of three-story building

(d) The damage on the column and BCJ component from the experimental program

Fig. 17 The stress distribution and damage scenario of the three-story building specimen

increment size in the 'Dynamic Implicit' method. Figs. 17(a)-(b) illustrate the Von Misses stress concentrations in the first-floor columns. As expected, the highest stress was experienced at the column bottoms and both extreme ends of the steel rebar and stirrup cage. Moreover, Fig. 17(c) depicts the concrete failure state after seismic force with the BCJ area, and the bottom end of the column experienced damage.

Results displaying the acceleration and displacement time histories of the FEA against the measured data are shown in Figs. 18 and 19, respectively. Both the acceleration and displacement time histories are in phase with the measured experimental data, and their amplitudes seem to be appropriately damped. The comparison value is within a reasonable amount of error and shows that the FE model can reproduce a reasonably match with the experimental results. While comparing the performance of linear and nonlinear results from Figs. 18 and 19, it can be found that the acceleration of linear analysis shows better comparison results to the shaking table test results. It verifies that the softer material properties of the floors are less obvious and the relative displacement results, shown in Fig. 19, mainly depended on the plasticity. Furthermore, when the seismic force exceeds the concrete stress, the displacement of the building specimen enters the plasticity and has a large deformation, which can be seen from the peak for each floor at the time of 25 seconds in Fig. 19.

Table 6 shows the maximum value of acceleration and

Table 6 Comparison of nonlinear dynamic FEA data to experimental data

Floor level	Direction	Max Acceleration (mm/s^2)		Max Displacement (mm)	
		Experimental	FEA	Experimental	FEA
Ground floor	Positive	9,441	9,359	-	-
	Negative	5,050	5,002	-	-
First floor	Positive	13,450	8,633	48	30
	Negative	14,602	6,149	47	78
Second floor	Positive	14,528	9,267	59	36
	Negative	16,210	6,751	58	87
Third floor	Positive	14,842	9,331	59	37
	Negative	17,049	6,790	58	88

displacement data for each floor under the seismic load given, which was taken from Figs. 18 and 19. The analysis using the NMSE method for the maximum acceleration and maximum relative displacement related in all the floor is 0.425 and 0.206, respectively. It can be found that this state of error is still tolerable.

4. Conclusions

This study focused on developing an FEA of the non-ductile detailing of the three-story RC building, including the column and BCJ components, which was previously
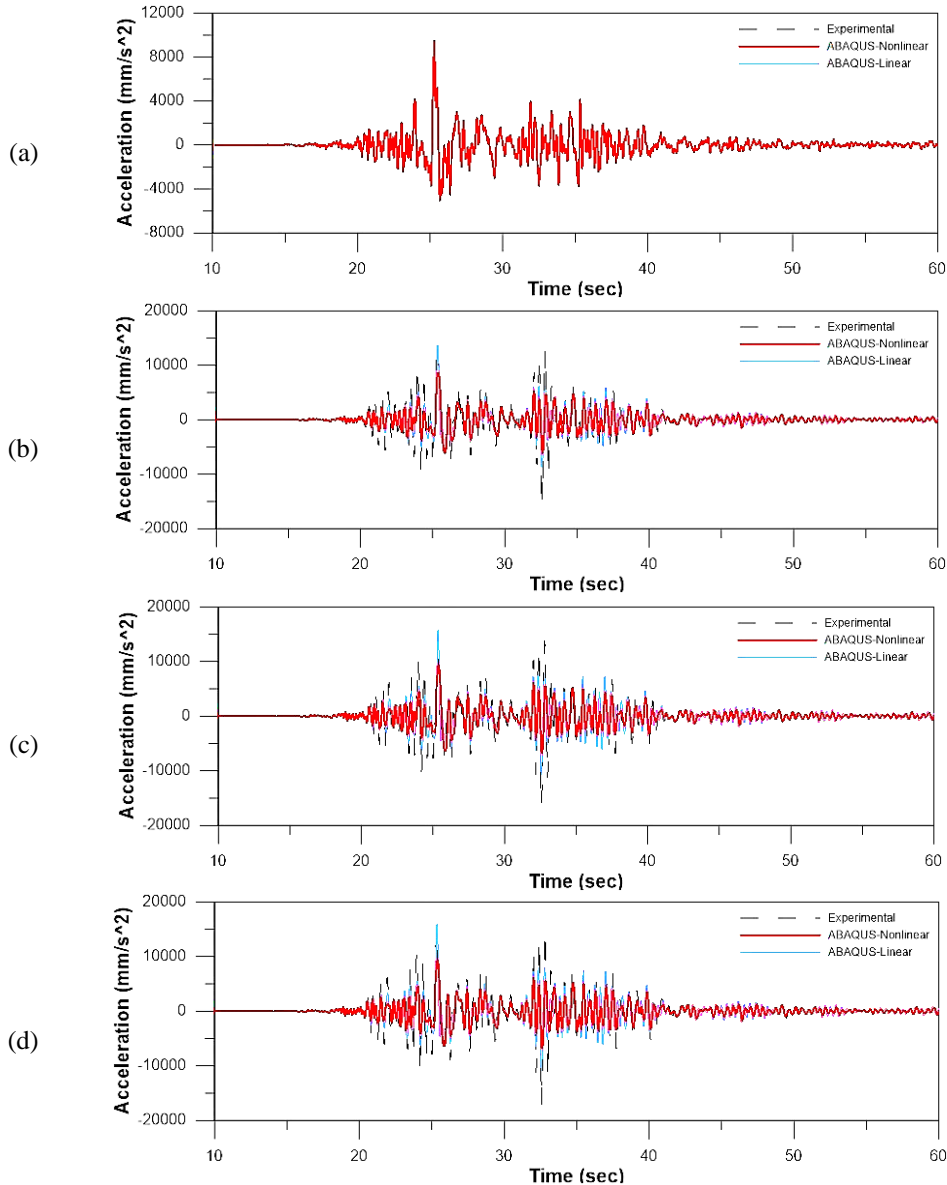
Fig. 18 Comparison of measured acceleration in nonlinear analysis at (a) ground floor; (b) first floor; (c) second floor; and (d) third floor

tested by the quasi-static test and the shaking table test in NCREE Taiwan. The numerical simulation was conducted by using the concrete damage plasticity model and represented the building collapsed during the earthquake.

The load-displacement graphs of the column and BCJ specimens were in a reasonable agreement for the numerical analysis and the experimental program. The initial stiffness and the ultimate load of the linear analysis result indicated to be in similar value. The damage scenario was also found in the bottom part of the column and the intersection joint between the beam with the column, respectively, for the column and BCJ specimens. Since the perfect bond assumption is used in the numerical model, there are still a room for improvement in the future work, which focuses on the contact interaction among the elements in the FEA model.

Furthermore, the findings of a dynamic analysis of the three-story building highlighted that an FE model can reproduce the experimental behavior with reasonable confidence. The errors obtained in accelerations and displacement results are acceptable compared to the experimental data. The highest stress concentration was also found at the column bottoms and both ends of the longitudinal and transversal reinforcements. The building failure was started from the BCJ area and the bottom end of the column, which was also found in the shaking table test results. The confinement effect related to the structure model needs to be further considered for future study.
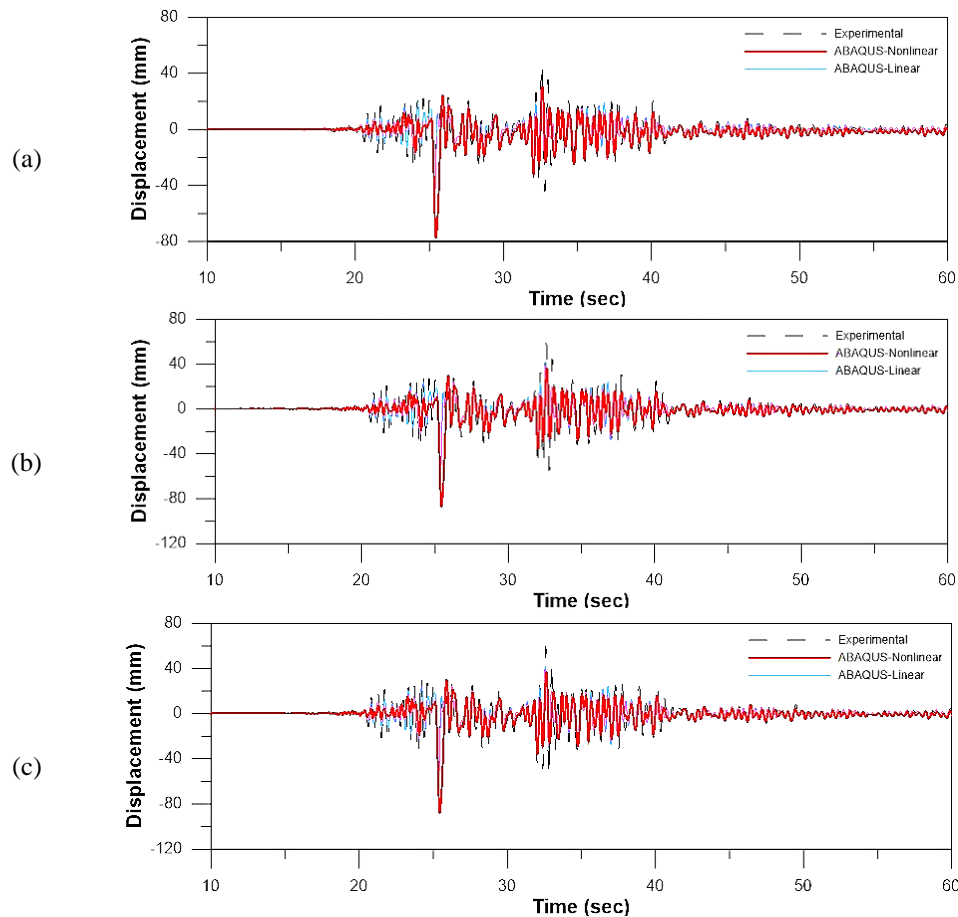
Acknowledgments

Fig. 19 Comparison of relative displacement in nonlinear analysis at (a) first floor; (b) second floor; and (c) third floor, with the ground floor

References

ACI 318 (2019), Building Code Requirements for Structural Concrete and Commentary, American Concrete Institute; Farmington Hills, MI, USA.

Castaldo, P., Gino, D. and Mancini, G. (2019), "Safety formats for non-linear finite element analysis of reinforced concrete structures: discussion, comparison and proposals", *Eng. Struct.*, **193**, 136-153. https://doi.org/10.1016/j.engstruct.2019.05.029.

Castaldo, P., Gino, D., Bertagnoli, G. and Mancini, G. (2020), "Resistance model uncertainty in non-linear finite element analyses of cyclically loaded reinforced concrete systems", *Eng. Struct.*, **211**, 110496. https://doi.org/10.1016/j.engstruct.2020.110496.

Celarec, D. and Dolšek, M. (2013), "The impact of modelling uncertainties on the seismic performance assessment of reinforced concrete frame buildings", *Eng. Struct.*, **52**, 340-354. https://doi.org/10.1016/j.engstruct.2013.02.036.

Cicekli, U., Voyiadjis, G.Z. and Abu Al-Rub, R.K. (2007), "A plasticity and anisotropic damage model for plain concrete", *Int. J. Plast.*, **23**(10-11), 1874-1900. https://doi.org/10.1016/j.ijplas.2007.03.006.

Dassault Systemes (2011), ABAQUS: Theory Manual, Dassault Systemes, Rhode Island, USA.

Design Specifications for Concrete Structures (2019), Ministry of the Interior, Taipei, Taiwan. (in Chinese)

Ghasemitabar, A., Rahmdel, J.M. and Shafei E. (2020), "Cyclic performance of RC beam-column joints enhanced with superelastic SMA rebars", *Comput. Concrete*, **25**(4), 293-302. http://doi.org/10.12989/cac.2020.25.4.293.

Hany, N.F., Hantouche, E.G. and Harajli, M.H. (2016), "Finite element modeling of FRP-confined concrete using modified concrete damaged plasticity", *Eng. Struct.*, **125**, 1-14. http://dx.doi.org/10.1016/j.engstruct.2016.06.047.

Haryanto, Y., Hu, H.T., Lie, H.A., Atmajayanti, A.T., Galuh, D.L.C. and Hidayat, B.A. (2019), "Finite element analysis of T-section RC beams strengthened by wire rope in the negative moment region with an addition of steel rebar at the compression block", *J. Teknol.*, **81**(4), 143-154. https://doi.org/10.11113/jt.v81.12974.

Hidayat, B.A., Hsiao, F.P., Hu, H.T., Lie, H.A., Pita, P. and Haryanto, Y. (2020), "Seismic performance of non-ductile detailing RC frames: an experimental investigation", *Earthq. Struct.*, **19**(6), 485-498. https://doi.org/10.12989/eas.2020.19.6.485.

Hidayat, B.A., Hu, H.T., Lie, H.A., Haryanto, Y., Widyaningrum, A. and Pramudji, G. (2019), "Nonlinear finite element analysis of traditional flexural strengthening using betung bamboo (Dendrocalamus asper) on concrete beams", *IOP Conf. Ser. Mater. Sci. Eng.*, **615**. https://doi.org/10.1088/1757-899X/615/1/012073.

Holický, M., Retief, J.V. and Sikora, M. (2016), "Assessment of model uncertainties for structural resistance", *Prob. Eng. Mech.*, **45**, 188-197. https://doi.org/10.1016/j.probengmech.2015.09.008.

Hu, H.T. and Schnobrich, W.C. (1990), "Nonlinear analysis of cracked reinforced concrete", *ACI Struct. J.*, **87**(2), 199-207.

Islam, A.B.M.S. (2020), "Computer aided failure prediction of reinforced concrete beam", *Comput. Concrete*, **25**(1), 67-73. https://doi.org/10.12989/cac.2020.25.1.067.

Jankowiak, T. and Lodygowski, T. (2005), "Identification of

parameters of concrete damage plasticity constitutive model", *Found. Civ. Environ. Eng.*, **6**, 53-69.

Kataoka, M.N., El Debs, A.L.H.C., Araujo, D.L. and Martins, B.G. (2020), "Computer modeling and analytical prediction of shear transfer in reinforced concrete structures", *Comput. Concrete*, **26**(2), 151-159. https://doi.org/10.12989/cac.2020.26.2.151.

Kepenek, E., Korkmaz, K.A. and Gencel Z. (2020) "Seismic risk investigation for reinforced concrete buildings in Antalya, Turkey", *Comput. Concrete*, **26**(3), 203-211. http://doi.org/10.12989/cac.2020.26.3.203.

Lin, J.L., Chen, W.H., Hsiao, F.P., Weng, Y.T., Shen, W.C., Weng, P.W., Li, Y.A. and Chao, S.-H. (2020), "Simulation and analysis of a vertically irregular building subjected to near-fault ground motions", *Earthq. Spectra*, **36**(3), 1485-1516. https://doi.org/10.1177/8755293020911134.

Ma, X., Ma, J. and Yue, Y. (2018), "Experimental and numerical investigation on seismic performance of a hybrid RC frame system with stiffened masonry wall", *J. Adv. Concrete Technol.*, **16**(12), 600-614. https://doi.org/10.3151/jact.16.600.

Mindess, S., Young, J.F. and Darwin, D. (2003), *Concrete*, 2nd Edition, Prentice-Hall, New Jersey, USA.

Otani, S. (2004), "Earthquake resistant design of reinforced concrete buildings: Past and future", *J. Adv. Concrete Technol.*, **2**(1), 3-24. https://doi.org/10.3151/jact.2.3.

Saenz, L.P. (1964), "Discussion of 'equation for the stress-strain curve of concrete' by Desayi and Krishnan", *J. ACI*, **61**, 1229-1235.

Shen, W.C., Hsiao, F.P., Tsai, R.J., Weng, P.W., Li, Y.A. and Hwang, S.J. (2019), "Shaking table test of a reduced scale reinforced concrete structure subjected to near-fault ground motion", *Proceedings of Pacific Conference on Earthquake Engineering*, Auckland, New Zealand, April.

Shen, W.C., Hsiao, F.-P., Weng, P.W., Li, Y.A., Chou, C.C. and Chung, L.L. (2018), "Seismic tests of a mixed-use residential and commercial building using a novel shaking table", *Proceedings of 11th US National Conference on Earthquake Engineering*, Los Angelos, USA, June.

Suwada, H. and Fukuyama, H. (2006), "Nonlinear finite element analysis on shear failure of structural elements using high performance fiber reinforced cement composite", *J. Adv. Concrete Technol.*, **4**(1), 45-57. https://doi.org/10.3151/jact.4.45.

Tien, Y.M., Juang, D.S., Pai, C.H., Hisao, C.P. and Chen, C.J. (2002), "Statistical analyses of relation between mortality and building type in the 1999 Chi-Chi earthquake", *J. Chin. Inst. Eng.*, **25**(5), 577-590. https://doi.org/10.1080/02533839.2002.9670732.

Tsai, K.C., Hsiao, C.P. and Bruneau, M. (2000), "Overview of building damages in 921 Chi-Chi earthquake", *Earthq. Eng. & Eng. Seism.*, **2**(1), 93-108.

Tsai, K.C. and Lin, M.L. (2002), "Seismic jacketing of RC columns for enhanced axial load carrying performance", *J. Chin. Inst. Eng.*, **25**(4), 389-402. https://doi.org/10.1080/02533839.2002.9670714.

Tudjono, S., Han, A.L. and Hidayat, B.A. (2015), "An experimental study to the influence of fiber reinforced polymer (FRP) confinement on beams subjected to bending and shear", *Procedia Eng.*, **125**, 1070-1075. https://doi.org/10.1016/j.proeng.2015.11.164.

Tudjono, S., Lie, H.A. and Gan, B.S. (2018), "An integrated system for enhancing flexural members' capacity via combinations of the fiber reinforced plastic use, retrofitting, and surface treatment techniques", *Int. J. Technol.*, **9**(1). https://doi.org/10.14716/ijtech.v9i1.298.

Wang, C.Y., Ho, H.Y., Wang, R.Z. and Huang, H.H. (2008), "Numerical simulations of non-ductile RC frames with infilled brick panel under cyclic loading", *J. Chin. Inst. Eng.*, **31**(5), 827-840. https://doi.org/10.1080/02533839.2008.9671436.

Yen, J.Y. and Chien, H.K. (2004), "Plated RC beam-column joints under cyclic loading", *J. Chin. Inst. Eng.*, **27**(5), 641-650. https://doi.org/10.1080/02533839.2004.9670912.

Yu, T., Teng, J.G., Wong, Y.L. and Dong, S.L. (2010), "Finite element modeling of confined concrete-I: Drucker-Prager type plasticity model", *Eng. Struct.*, **32**(3), 665-679. https://doi.org/10.1016/j.engstruct.2009.11.014.

Zepeda, D. and Hagen, G. (2016), "Lessons learned from the 2016 Taiwan Mei-Nong earthquake", *Proceedings of Structural Engineers Association of California Convention*, Taipei, Taiwan, October.

Bechtoula, H. and Ousalem, H. (2005), "The 21 May 2003 Zemmouri (Algeria) earthquake: damages and disaster responses", *J. Adv. Concrete Technol.*, **3**(1), 161-174. https://doi.org/10.3151/jact.3.161.

CC